

Dimensionality-tuned electronic structure of nickelate superlattices explored by soft-x-ray angle resolved photoelectron spectroscopy

G. Berner,¹ M. Sing,¹ F. Pfaff,¹ E. Benckiser,² M. Wu,² G. Christiani,² G. Logvenov,² H.-U. Habermeier,² M. Kobayashi,³ V.N. Strocov,³ T. Schmitt,³ H. Fujiwara,⁴ S. Suga,⁵ A. Sekiyama,⁵ B. Keimer,² and R. Claessen¹

¹*Physikalisches Institut and Röntgen Center for Complex Material Systems (RCCM), Universität Würzburg, Am Hubland, D-97074 Würzburg, Germany*

²*Max Planck Institute for Solid State Research, Heisenbergstrasse 1, D-70569 Stuttgart, Germany*

³*Swiss Light Source, Paul Scherrer Institut, CH-5232 Villigen, Switzerland*

⁴*Division of Materials Physics, Graduate School of Engineering Science, Osaka University, Osaka 560-8531, Japan*

⁵*Institute of Scientific & Industrial Research, Osaka University, Ibaraki, Osaka 567-0047, Japan*

(Dated: August 29, 2021)

The electronic and magnetic properties of epitaxial LaNiO₃/LaAlO₃ superlattices can be tuned by layer thickness and substrate-induced strain. Here, we report on direct measurements of the k -space-resolved electronic structure of *buried* nickelate layers in superlattices under compressive strain by soft x-ray photoemission. After disentangling strong extrinsic contributions to the angle-dependent signal caused by photoelectron diffraction, we are able to extract Fermi surface information from our data. We find that with decreasing LaNiO₃ thickness down to two unit cells (2 uc) quasiparticle coherence becomes strongly reduced, in accord with the dimension-induced metal-to-insulator transition seen in transport measurements. Nonetheless, on top of a strongly incoherent background a residual Fermi surface can be identified in the 2 uc superlattice whose nesting properties are consistent with the spin-density wave (SDW) instability recently reported. The overall behavior of the Ni 3d spectra and the absence of a complete gap opening indicate that the SDW phase is dominated by strong order parameter fluctuations.

PACS numbers: 79.60.-i, 79.60.Jv, 73.20.-r, 73.50.Pz

I. INTRODUCTION

Artificial heterostructures made from transition metal oxides may host novel electronic and magnetic phases not present in the bulk of the constituents. Such phases may be controlled by, *e.g.*, elastic strain or interfacial charge transfer.¹ In this context the perovskite LaNiO₃ (LNO) is a very interesting material, as it is the only member of the $RENiO_3$ ($RE =$ rare earth, *viz.*, La, Pr, Nd, Sm, Eu) family showing metallic behavior with its partially-filled degenerate Ni 3d e_g (d_{z^2} and $d_{x^2-y^2}$) orbitals, while the other compounds exhibit a correlation-driven metal-insulator (MI) transition at low temperatures.^{2,3} LNO is thus a highly correlated metal being close to an insulating phase, which may be switchable by interfacing.

Indeed, recent investigations have shown that the physical properties of LNO can be tuned by reducing its dimensionality or applying strain. For instance, density functional theory (DFT) calculations found that a single unit cell (uc) of LNO sandwiched between layers of the band insulator LaAlO₃ (LAO) and thus under tensile strain displays a cuprate-like Fermi surface, identifying LNO as a possible candidate for exotic superconductivity.⁴⁻⁶ Inspired by these predictions a large number of experimental and theoretical studies have been performed on ultra-thin films and superlattices (SLs).⁷⁻²¹

Experimentally, ultra-thin films are found to exhibit a dimensional crossover from metallic to insulating behavior upon reducing the film thickness, with critical values ranging from 3 to 9 uc⁷⁻¹⁰. The situation is slightly dif-

ferent in LNO-based SLs: while thicker LNO layers embedded in SL structures remain metallic at all temperatures, 2 uc layers display a temperature-dependent MI transition.¹² The critical temperature depends mainly on the epitaxial strain induced by the substrate. The strain also leads to a distortion of the octahedral ligand field and hence a lifting of the e_g orbital degeneracy. The resulting orbital polarization increases almost linearly with the induced strain.^{17,18} The reason for the appearance of the insulating state in both SLs and ultra-thin films is still under debate. Different scenarios like Anderson localization,^{7,8} Mott insulator transition,^{5,6} charge disproportionation,^{13,22} and spin density wave^{12,17} have been discussed.

It should be noted that in superlattices the necessity of octahedral connectivity across the interfaces in combination with strain induced by the substrate can stabilize different distortions compared to the situation in epitaxial films.^{23,24} We emphasize in particular that in comparison to ultrathin films the superlattice structures allow for a better defined and efficient control of the strain effects. Since LNO with its LaO⁺ and NiO₂⁻ sublayers is polar, the (001)-oriented free surfaces of thin LNO films tend to reconstruct structurally by polar distortions or octahedral rotations to minimize the electrostatic energy.²⁴⁻²⁶ The modified structure results in a change of the electronic structure, at least near the surface. In contrast, the LNO layers in the SLs are embedded in LAO, a host material of like polarity, and are thus stabilized against structural effects resulting from polar discontinuities, as shown by x-ray diffraction.²⁶

Thus, the physical properties of the strained LNO layers and their dependence on dimensionality can be studied under clean conditions, *i.e.*, in the absence of additional ionic or electronic surface and interface reconstructions

Direct insight into the electronic structure can be achieved by photoelectron spectroscopy (PES). Many of the scenarios mentioned above are reflected directly or indirectly in the microscopic electronic structure, *i.e.*, in the single-particle spectral function, to which PES provides direct access. Such investigations have focused so far on (ultra-thin) films by angle-integrated⁹ as well as angle-resolved PES (ARPES).^{10,27,28} However, ARPES studies on SLs require a more bulk-sensitive approach, since the LNO layers are buried below several unit cells of the host material (LAO in our case). Conventional photoemission with low-energy photons is limited by its very low information depth of a few Angstroms only, determined by the photoelectron mean free path (MFP) and therefore cannot easily access the LNO layers. In contrast, photons in the soft x-ray (SX) regime allow for higher MFP at still reasonable momentum resolution (k -resolution), thereby enabling k -resolved probing of the buried electronic structure in such SLs.^{29,30}

In this study, we present SX-ARPES measurements on LNO/LAO SLs under compressive strain and a detailed analysis of the buried electronic structure. Besides a significant loss of quasiparticle (QP) coherence near the Fermi level (E_F) for the two-dimensional ground state, observed in the angle-integrated valence band spectra, our k -resolved measurements trace the dimensional crossover from a three-dimensional Fermi surface in the 4 uc LNO-SL to two-dimensional behavior in the 2 uc LNO-SL. Although the intensity distribution in our k -space maps is strongly affected by x-ray photoelectron diffraction (XPD), we are able to extract bandstructure information on the Ni $d_{x^2-y^2}$ -derived hole pocket states in all LNO/LAO SLs. An indication of the Ni d_{z^2} -derived electron pocket is only observed in the 2 uc LNO-SL. The residual Fermi surface observed in this sample displays strong nesting properties which are consistent with the spin-density wave (SDW) scenario recently put forward as explanation for the insulating low-temperature ground state.

II. EXPERIMENT

LNO/LAO superlattices with different LNO layer thickness were grown by pulsed laser deposition on (001) LaSrAlO₄ (LSAO) single crystal substrates. The deposition starts with a number of N ($=2, 4$) unit cells of LNO followed by the same number of LAO layers. This stacking sequence ($N//N$) is repeated fifteen and eight times for $N=2, 4$, respectively, terminating with an LAO layer at the surface [see Fig. 1 (a)]. Additionally, a (10//4) \times 4 SL was prepared being used as a thick LNO reference layer, also capped by 4 uc LAO.

The LNO/LAO stacks are compressively strained to the LSAO substrate, since the lattice mismatch between the LSAO and bulk pseudo-cubic LNO ($a = 3.838$ Å)³¹ is $\approx -3.2\%$ (Ref. 18). The induced biaxial strain, which is stable up to a SL thickness of ≈ 50 nm (Ref. 32), was confirmed by x-ray diffraction with lattice parameters $a = 3.750$ Å and $c = 3.840$ Å (Ref. 18).

The photoemission experiments were performed at the ADDRESS beamline of the Swiss Light Source with a SPECS Phoibos 150 spectrometer using p -polarized photons.^{30,33} The overall energy resolution was 70 meV at a photon energy of 700 eV. During the experiment the samples were cooled down to $T = 11$ K. Preliminary SX-ARPES experiments were performed at beamline BL25SU, SPring-8, Japan, to establish the feasibility of the method. Prior to the measurements the sample surface was cleaned by keeping the samples under ozone flow for 45 min, followed by an *in situ* annealing at 180°C under 1×10^{-5} mbar of oxygen for 45 min. This method was found to strongly suppress the amount of carbon-containing surface contaminants.

III. RESULTS

A. Angle integrated spectra

Figure 1 (b) shows the angle integrated valence band (VB) spectra of the (2//2), (4//4), and (10//4) SLs measured in normal emission geometry at low temperature ($T = 11$ K). Below -2 eV the valence band mainly consists of superposed LAO and LNO O $2p$ -derived states. Due to the valence band offset of ≈ 2 eV between LAO and LNO (see Appendix A) the spectral weight between -2 eV and E_F can unambiguously be assigned to LNO states, in particular to the crystal-field split Ni $3d$ t_{2g} and e_g states at ≈ -0.8 eV and at E_F , respectively. The octahedral splitting is consistent with values observed in thin LNO films.^{9,15,34} The spectra are normalized to the same integrated area between -2 eV and E_F in order to facilitate easy identification of the changes in the Ni $3d$ states in this energy window. A normalization to the integral intensity of the *full* valence band (between -10 eV and E_F) would not provide a meaningful comparison because of the superimposed LAO and LNO valence band contributions, whose relative intensities strongly change for different layer thicknesses due to the finite probing depth.

In the VB spectra of the (4//4) and (10//4) SL the e_g derived feature shows a clear cut-off by the Fermi-Dirac-function at E_F signalling that the samples remain metallic at low temperature down to a LNO layer thickness of 4 uc. This is consistent with electrical transport measurements shown in Fig. 1 (c) and recent results from optical ellipsometry on the same SLs.¹²

In comparison, the VB spectrum of the (2//2) SL displays a remarkable change near the Fermi level: No Fermi edge can be identified, instead both the t_{2g} and e_g fea-

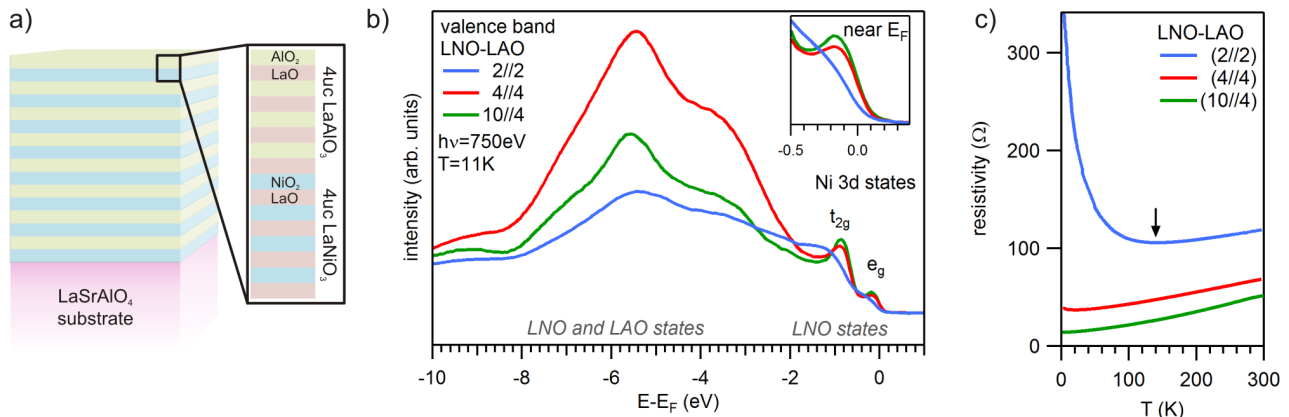


FIG. 1. (Color online) (a) Layout of the (4//4) LNO/LAO superlattice. The first LNO layer is buried below four uc LAO. (b) k -integrated valence band spectra of the investigated LNO/LAO samples at low temperature. The (2//2) SL exhibits a dramatic loss of quasiparticle coherence at the Fermi level (see inset). The spectra are normalized to the same integrated area between -2 eV and E_F . (c) Temperature-dependent resistivity measurements. The (2//2) SL shows a continuous MI transition at $T \approx 150$ K, while the (4//4) and (10//4) SLs stay metallic down to very low temperatures.

tures are smeared out indicating a loss of quasiparticle coherence. In contrast to a recent photoemission study of ultra-thin films⁹ our VB spectrum does not show a full band gap opening, but a distinct reduction of spectral weight at the Fermi level. Corresponding four point probe transport measurements of the identical samples confirm an insulating phase at low temperature and a temperature dependent MI crossover at $T \approx 150$ K driven by the reduced dimensionality [see arrow in Fig. 1 (c)]. For very thin LNO layers such a transition has only been observed in SL structures, but not in films.^{12,26}

B. k -resolved spectra

The angle-integrated spectra already demonstrate the pronounced effect of reduced LNO layer thickness on the electronic structure. In the following we study this in more detail by using the k -space resolved spectra, in particular with respect to Fermi surface (FS) volume and topology. For the interpretation of the measured data it is helpful to start the discussion from the theoretical FS obtained by DFT calculations. Figure 2 shows cuts through the expected three-dimensional FS of bulk LNO parallel to the surface ($k_z = 0 \text{ \AA}^{-1}$ and $\frac{\pi}{c}$, k_z denoting the wavevector component perpendicular to the surface) as well as the k_z -independent two-dimensional FS of a single LNO layer (calculated without (c) and with (d) correlation effects), based on Refs. 35 and 5, respectively. In the case of bulk LNO the Ni d_{z^2} states form an electron pocket at the Brillouin zone (BZ) center (Γ point) [cf. Fig. 2 (a)], while the Ni $d_{x^2-y^2}$ orbitals create large hole pockets at the zone corners (A points) [cf. Fig. 2 (b)]. By reducing the LNO layer thickness, the three-dimensional FS transforms into a two-dimensional one, where both the electron and hole pockets are present [cf.

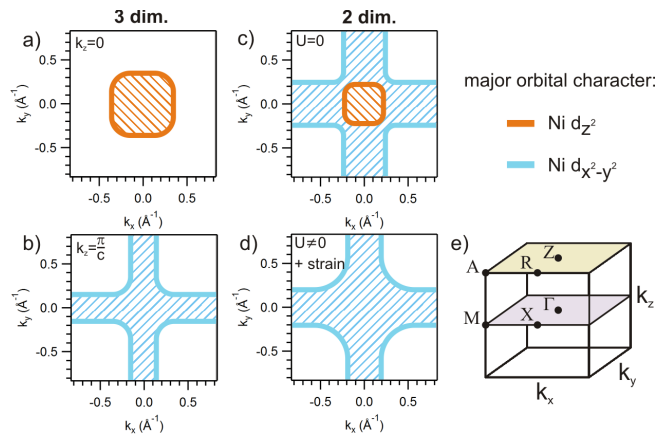


FIG. 2. (Color online) Schematic cuts (solid lines) through the three-dimensional Fermi surface of bulk LNO at (a) $k_z = 0 \text{ \AA}^{-1}$ and (b) $k_z = \frac{\pi}{c}$ as well as the k_z -independent two-dimensional FS (c) without and (d) including correlation effects (symbolized in the figure by zero and non-vanishing on-site Coulomb repulsion energy U) and tensile strain according to Ref. 35 and 5, respectively. The shaded areas indicate the occupied states. (e) Drawing of the cubic Brillouin zone including the high-symmetry points.

Fig. 2 (c)]. Hansmann *et al.* showed that under tensile strain and influence of correlation effects the d_{z^2} states can be lifted above the Fermi level and fully depopulated [cf. Fig. 2 (d)].

We begin our analysis of the k -resolved data by investigating the spectra taken with a photon energy of 710 eV, which corresponds to a k -space cut at $k_z = \frac{\pi}{c}$ (see Appendix B). Here the hole pockets should always be observable, independent of dimensionality or possible strain- or correlation-induced orbital polarization. Fig. 3 (a) and (c) show the energy distribution

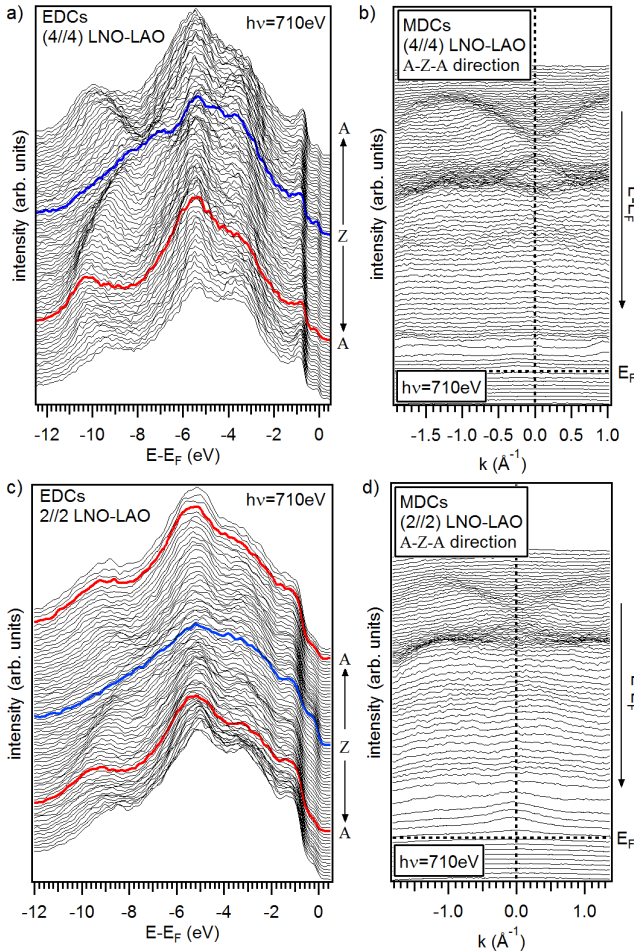


FIG. 3. (Color online) (a), (b) The energy and momentum distribution curves (EDCs) and MDCs) of the (4/4) SL taken in A-Z-A direction show at lower energies strongly dispersive O $2p$ derived bands. (c), (d) These bands are also detectable in the EDCs and MDCs of the (2/2) SL measured in same direction. The observation of dispersive bands confirms the high crystalline quality of both SL and allows the identification of the high-symmetry points.

curves (EDCs) and (b) and (d) the corresponding momentum distribution curves (MDCs) of the (4/4) and (2/2) sample, respectively, along the A-Z-A direction of the BZ. Strongly dispersive O $2p$ -derived bands are observed in both samples at lower energies between -8 to -10 eV, indicating the high-quality crystalline structure of our SLs. Furthermore, the periodic band dispersion allows a clear identification of the high symmetry points Z at $k_{\parallel} = 0 \text{ \AA}^{-1}$ and A at $k_{\parallel} = \frac{\pi}{a}$. The superposition of LAO and LNO states between -8 and -2 eV hinders the detection of dispersions of the O $2p$ -derived bands in this region. Near E_F one can clearly identify the Ni $3d$ states, although their intensity is much lower in comparison to the O $2p$ -derived valence states.

A more detailed view on the Ni $3d$ states near the Fermi level is given in Fig. 4 (a) and (b), where the

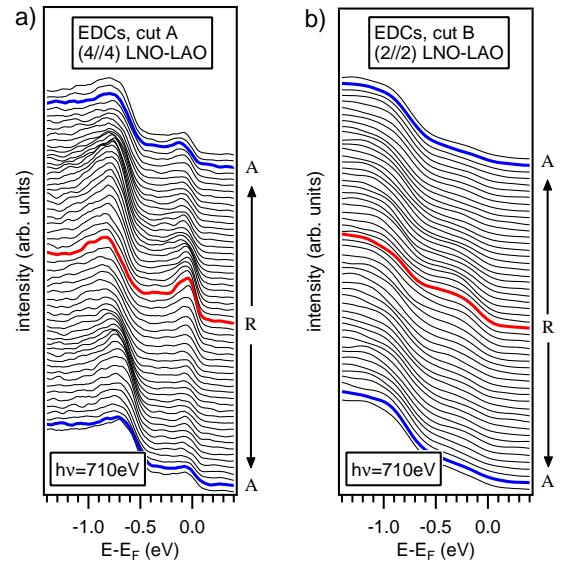


FIG. 4. (Color online) EDCs near E_F measured along two cuts — labelled A and B — in A-R-A direction. The locations of both cuts are indicated in Fig. 6. (a) The EDCs of the (4/4) SL exhibit no dispersion in the hole pocket states around R within experimental resolution. (b) Both the Ni t_{2g} and e_g states of the (2/2) SL are smeared out due to the loss of QP coherence. Only a residue of k -dependent intensity can be found near R.

EDCs taken in A-R-A direction are shown for both samples. Interestingly, a large fraction of k -independent intensity at the Fermi level is found. This loss of momentum information may be explained by non-direct transitions due to polaronic effects, as also reported for other oxide compounds.^{36,37} Nevertheless, there is residual k -dependent intensity modulation at the Fermi level in both samples (though of different strength), consistent with the expected Fermi level crossing of the $d_{x^2-y^2}$ band along A-R-A [cf. Fig. 2]. The EDCs of the (4/4) SL [see Fig. 4 (a)] exhibit an intense structure around R which can be assigned to the occupied states between the hole pockets. However, while Eguchi *et al.* found at this high-symmetry point a clearly dispersive band in their SX-ARPES study of a thick LNO film under comparable experimental conditions²⁷, no dispersion is discernible in our measurement, already indicating a deviation of the SL from the bulk band structure.

In comparison to the (4/4) SL, where the Ni t_{2g} and e_g states are well separated in energy, both features are considerably smeared out in the (2/2) SL [see Fig. 4 (b)]. Since the SL is well ordered as proven by the distinct dispersions in the O $2p$ valence band, we attribute this behavior to the pronounced loss of QP coherence, as already discussed above. The reduced QP coherence furthermore prevents the identification of possible dispersive structures. An only very weak, but significant intensity modulation around the R point may be interpreted as a remnant of the occupied $d_{x^2-y^2}$ band states sitting on

top of a largely k -independent incoherent background.

C. X-ray photoelectron diffraction

Figures 5 (a)–(e) show angle-resolved photoelectron distribution maps measured at different fixed binding energies (constant energy maps). The experimental geometry is sketched in Fig. 5 (f), where the angles θ and ϕ are rotation angles around the sample axes as indicated and describe the direction of photoelectron emission with respect to the surface normal.³⁰ By adjusting θ and ϕ a two-dimensional cut in momentum space, spanned by \mathbf{k}_{\parallel}^a and \mathbf{k}_{\parallel}^b , can be sampled (in our experiments the sample orientation was such that the k_x and k_y axes, defining the first Brillouin zone as in Fig. 2, were rotated by 45° with respect to \mathbf{k}_{\parallel}^a and \mathbf{k}_{\parallel}^b). For the special case $\phi = 0^\circ$, the relation between the initial state momentum component parallel to the sample surface, k_{\parallel}^a , and θ is given by the following equation:

$$k_{\parallel}^a = \frac{\sqrt{2m_e}}{\hbar} \sqrt{E_{\text{kin}}} \sin \theta - k_{\parallel}^{\text{ph}}, \quad (1)$$

where m_e is the free electron mass and E_{kin} the kinetic energy of the photoelectrons. $k_{\parallel}^{\text{ph}}$ denotes the parallel component of the photon momentum $p^{\text{ph}} = \hbar k^{\text{ph}} = \frac{h\nu}{c}$, which is transferred to the emitted photoelectron [see Fig. 5 (g)]. While this contribution can be neglected in low-energy ARPES measurements ($h\nu < 100$ eV), it has to be taken into account in SX-ARPES when converting the angular scale to momentum scale. Note that in the given geometry a correction only for the θ -axis is sufficient, since the variation of $\phi \neq 0^\circ$ is small and thus the lateral contribution of the photon momentum is negligible.

Figure 5 (a) and (b) show the constant energy maps of the (4//4) SL at the Fermi level (e_g states) and at $E = -0.8$ eV (t_{2g} states) integrated over energy windows of ± 0.15 eV and ± 0.30 eV, respectively. Note that only part of the full intensity range is captured by the color scale as is indicated for each map. Remarkable intensity modulations are observed in the map of the e_g states. A more detailed analysis may be obtained from the angle-dependent measurements of the t_{2g} states in Fig. 5 (b): The chosen integration range corresponds roughly to the bandwidth of the fully occupied t_{2g} states, and hence the spectral weight distribution should simply reflect the momentum distribution function $n(\vec{k})$ which for a completely occupied band is constant = 1. However, strong intensity modulations are clearly observable exhibiting a geometric symmetry with respect to $\theta = 0^\circ$ [cf. Fig. 5 (f)] but none with respect to any high-symmetry point or line in k -space. This suggests that most of the intensity modulation may be attributed to x-ray photoelectron diffraction (XPD).³⁸ Here, the excited photoelectron is viewed as a spherical wave originating at some emitting atom and elastically scattered off the neighboring atoms

in the lattice. Interference results in an intensity pattern which is symmetric in the *angle coordinates* while modulations due to the electronic structure are symmetric in *momentum space*. Note that for the high kinetic energies used here forward scattering dominates the XPD process.³⁹ The appearance of this effect in SX-ARPES measurements has been reported also for other oxide SL systems.⁴⁰

The angular intensity distribution of the e_g photoemission map is additionally affected by the only partial k -space occupation of the e_g states, leading to the strongly reduced signal at small angles (with some remaining non-zero incoherent background). XPD effects are nonetheless well visible in the occupied part of the Brillouin zone, *e.g.*, as pronounced intensity maxima at $\theta \approx 10^\circ$ (such as seen also in the t_{2g} maps).

The identification of XPD as origin of the intensity modulations in the Ni $3d$ states is supported by angle-resolved data of the Ni $3p$ core level at $E = -67$ eV [see Fig. 5 (c)]. The data were taken at a photon energy of $h\nu = 780$ eV in order to ensure the same kinetic energy, *i.e.*, same wave length, as in the ARPES maps in Fig. 5 (a) and (b). The Ni $3p$ XPD pattern — since core-levels are dispersionless, without intensity modulations owing to a momentum-dependence of the electronic structure — shows clear structure-induced symmetries about $\theta = 0^\circ$ and $\phi = 0^\circ$ and contains many of the features also seen in the Ni $3d$ maps.

We observe similar intensity distributions in the angle-resolved maps of the e_g - and t_{2g} states of the (2//2) SL, as shown in Fig. 5 (d) and (e), respectively. While the map of the fully occupied t_{2g} band again exhibits clear XPD-induced symmetry with respect to $\theta = 0^\circ$, the map of the e_g states displays a superposition of k -dependent state occupancy, *e.g.*, the X-shaped structure at $k_{\parallel}^{a,b} = 0 \text{ \AA}^{-1}$, and XPD-induced modulations, *e.g.*, at $\theta \approx 10^\circ$.

The difference in the observed intensity modulations between both SLs at E_F is explained on the one hand by the k -dependent occupancy of the Ni e_g states (see discussion in the next section). On the other hand the different layer thicknesses of LAO and LNO may lead to slightly different XPD modulation patterns, especially in the angle-resolved intensity distribution maps of the t_{2g} states.

D. Fermi surfaces

After having separated out the angular XPD effects in the photoemission maps taken at E_F (e_g states) we now turn to the underlying k -dependent structures resulting from the electronic structure, *i.e.*, the Fermi surface of the buried LNO layers. For better identification we compare the measured intensity distributions, provided with a momentum scale, with the calculated Fermi surfaces in Fig. 6.

Starting with the (4//4) SL [Fig. 6 (a)], recorded at

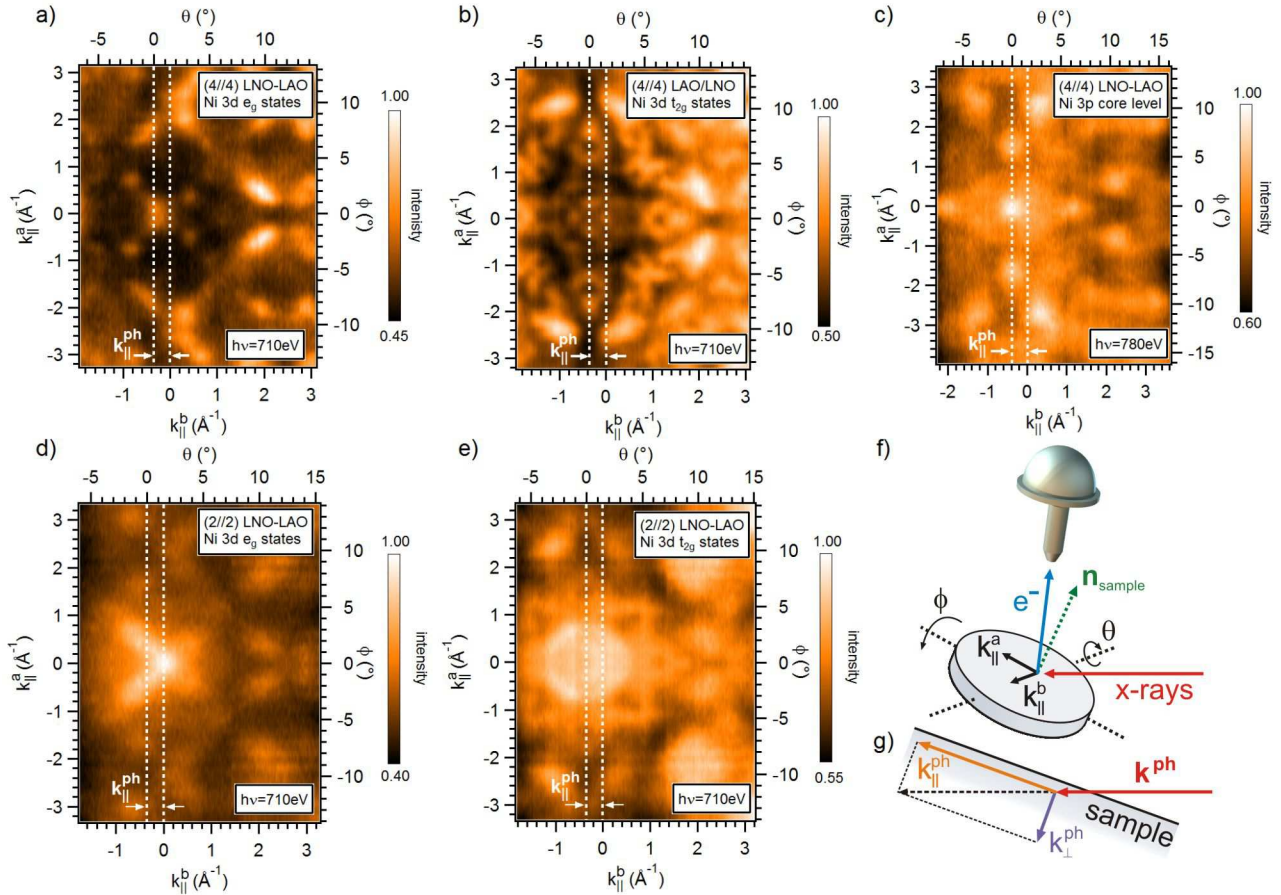


FIG. 5. (Color online) Angle-resolved constant energy maps of the (4//4) and (2//2) SL measured at different binding energies. Only part of the full intensity range is captured by the color scale as is indicated for each map. (a) The map of the (4//4) SL at E_F (e_g states) exhibits strong intensity modulation. (b) The intensity map measured at -0.8 eV (t_{2g} states) displays symmetry with respect to $\theta = 0^\circ$. Thus, the observed modulations may be identified as a result of photoelectron diffraction. (c) Angle-resolved measurements of the Ni $3p$ core level, taken at a similar kinetic energy as the valence band maps in (a) and (b), show a comparable pattern. (d),(e) The angle-resolved data of the e_g (d) and t_{2g} states (e) taken on the (2//2) SL provide similar results. It should be noted that the figures of the (2//2) SL were made by mirroring the data at $\phi = 0^\circ$, which does not reduce the information on the FS, since the line $\phi = 0^\circ$ corresponds to a real mirror plane of the experiment. (f) Schematic view of the experimental geometry. (g) The projection of the soft x-ray photon momentum parallel and perpendicular to the sample surface at arbitrary θ and $\phi = 0^\circ$.

$h\nu = 710$ eV, which in the free-electron approximation for the final states corresponds to $k_z = \frac{\pi}{c}$, we find qualitatively very good agreement with the calculated k -space occupation at this very k_z (gray shaded schematic). In particular, the hole pockets around the A points are clearly visible. As already discussed above, due to the moderate resolution of the experiment no sharp Fermi-level crossings of the dispersing bands can be observed. With the energy integration range (± 0.15 eV) being comparable to the e_g band width these maps essentially reflect the momentum distribution function $n(\vec{k})$, *i.e.*, the occupied k -space between the hole pockets rather than the FS contours [cf. shaded areas in Fig. 6 (a)].⁴¹

The Fermi level intensity map of the (2//2) SL shown in Fig. 6 (b) basically resembles the expected momentum distribution function in the two-dimensional limit.

Compared to the data of the (4//4) SL the structures are broader in k -space. This can be explained by the change of the FS from the three-dimensional to the two-dimensional topology, where the hole pockets have to shrink in order to keep the Fermi volume constant [cf. Fig. 2], resulting in a broader occupied k -space region between the hole pockets. At the Z point of the first BZ of the (2//2) SL some additional intensity is clearly visible, but much less so in higher-order zones, possibly due to matrix element effects. It is tempting to assign this intensity to the additional electron pocket in the center of the BZ predicted for the two-dimensional limit of Fig. 2 (c). That this intensity maximum is clearly centered around $k_{||}^{x,y} = 0 \text{ \AA}^{-1}$ (and not $\theta = 0^\circ$, see Fig. 5 (d)) supports the interpretation as genuine part of the band structure and rules out an XPD effect.

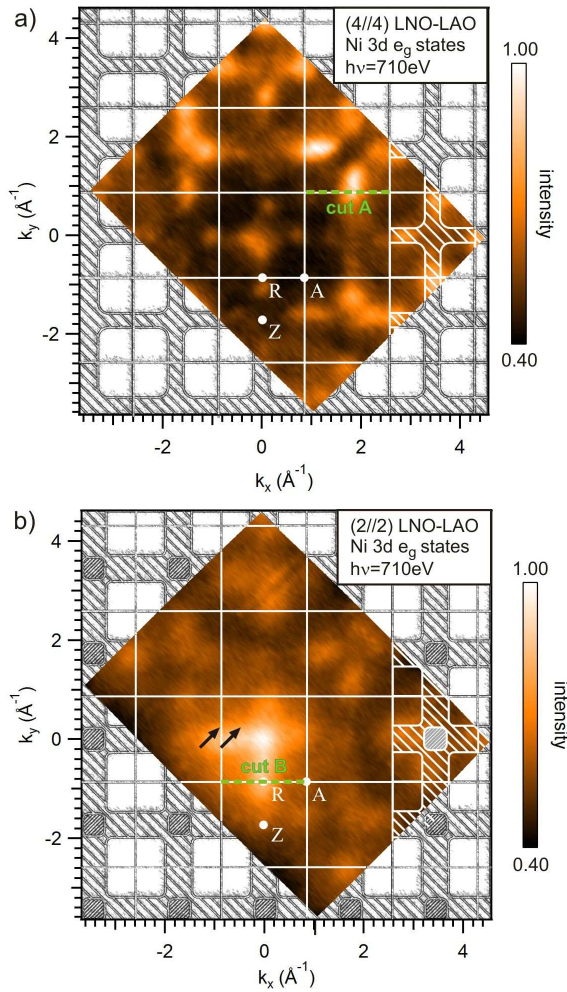


FIG. 6. (Color online) (a) The k -resolved intensity distribution map of the (4/4) SL taken at E_F with $k_z = \frac{\pi}{c}$ (710 eV) including several BZs shows the distinct hole pockets around the A points, in line with band theory (shaded drawings). (b) The k -resolved map of the (2/2) SL is in good agreement with the k_z -independent two-dimensional FS with hole pockets around the A points and an additional electron pocket around the Z point. The latter one is only clearly observable at $k_{x,y} = 0 \text{ \AA}^{-1}$, presumably due to matrix element effects. The arrows indicate a possible nesting vector of the FS, which agrees with the SDW wave vector $\mathbf{Q}_{SDW} = 2\pi(\frac{1}{4}, \frac{1}{4}, 0)$. The lines A and B denote the k -space cuts probed by the EDCs in Fig. 4. The intensity of both maps is normalized to that at $k_{x,y} = 0 \text{ \AA}^{-1}$.

Both maps are taken at $k_z = \frac{\pi}{c}$. Since for a three-dimensional, *i.e.*, bulk-like, FS the electron pocket should only be visible at the Γ -points (corresponding to integer multiples of $\frac{2\pi}{c}$ in k_z direction within the extended zone scheme), as can be seen from the theoretical FS in Fig. 2, it is interesting to look at FS cuts containing a Γ point. The next available Γ -point requires a photon energy of $h\nu = 630$ eV (see Appendix B). The intensity distribution map of the (2/2) SL shown in Fig. 7 (a) indeed exhibits significant intensity at the Γ point, which may be

a result of overlapping intensity derived from the Ni d_{z^2} states at Γ and XPD-induced modulations at $\theta = 0^\circ$. The diffuse intensity distribution towards the BZ edge may be interpreted as residual spectral weight of the occupied states between the hole pockets, although the very low Fermi level intensity prevents a more detailed analysis. In any case, the ubiquity of the zone center intensity for all photon energies (and thus its k_z -independence) strongly supports the two-dimensional character of the FS in the (2/2) SL.

Figure 7 (b) shows the Fermi surface maps taken on the (4/4) SL at $h\nu = 630$ eV. Due to the thicker LNO layer one would expect to slowly recover bulk behavior with a stronger electron pocket signal at the Γ point. However, we found no evidence for a k -dependent state occupancy in our data. Rather, all intensity modulations exhibit a symmetry with respect to $\theta = 0^\circ$, identifying them as XPD-induced structures. To verify this result, we additionally performed angle-resolved measurements on the (10/4) SL at the same photon energy, since at 10 uc LNO layer thickness a closer approach to a fully established three-dimensional FS can be expected.¹⁰ However, also in this SL no significant k -dependent structures are detected, in particular, no electron pocket is found at the Γ point [see Fig. 7 (c)]. Furthermore, a k -space scan in k_z direction by varying the photon energy from 580 to 820 eV (not shown here) did not reveal any signal which could be assigned to the Ni d_{z^2} pocket around $k_{\parallel}^{a,b} = 0 \text{ \AA}^{-1}$.

IV. DISCUSSION

The SX-ARPES data taken for $k_z = \frac{\pi}{c}$ ($h\nu = 710$ eV) provide direct spectroscopic evidence of the predicted Ni $d_{x^2-y^2}$ -derived hole pockets in all investigated SL. However, for the electron pocket formed by Ni d_{z^2} states in the BZ center indications are only found in the (2/2) SL. The angle-resolved data of both the (4/4) SL and (10/4) SL taken in the central plane of the BZ ($k_z = 0 \text{ \AA}^{-1}$, *i.e.* $h\nu = 630$ eV) are strongly affected by XPD-induced intensity modulations and display no clear k -dependent state occupancy. This is a surprising result, because a recent SX-ARPES study on *thick* LNO films has reported clear evidence of the Ni d_{z^2} states and their three-dimensional dispersion.²⁷

It may be tempting to attribute this difference between confined LNO layers in SLs and bulk LNO to the strain induced by the substrate. However, a recent resonant reflectometry study focussing on the correlation between strain and orbital polarization in LNO/LAO SLs provides evidence that compressive strain enhances the Ni d_{z^2} bandfilling compared to the situation in unstrained LNO.^{11,18} Conversely, tensile strain energetically lifts the d_{z^2} orbital and causes its depopulation. This trend is supported by DFT calculations for ultra-thin LNO films⁴² and superlattices.^{5,6,43,44} Thus, the scenario that compressive strain induced by the LSAO substrate pos-

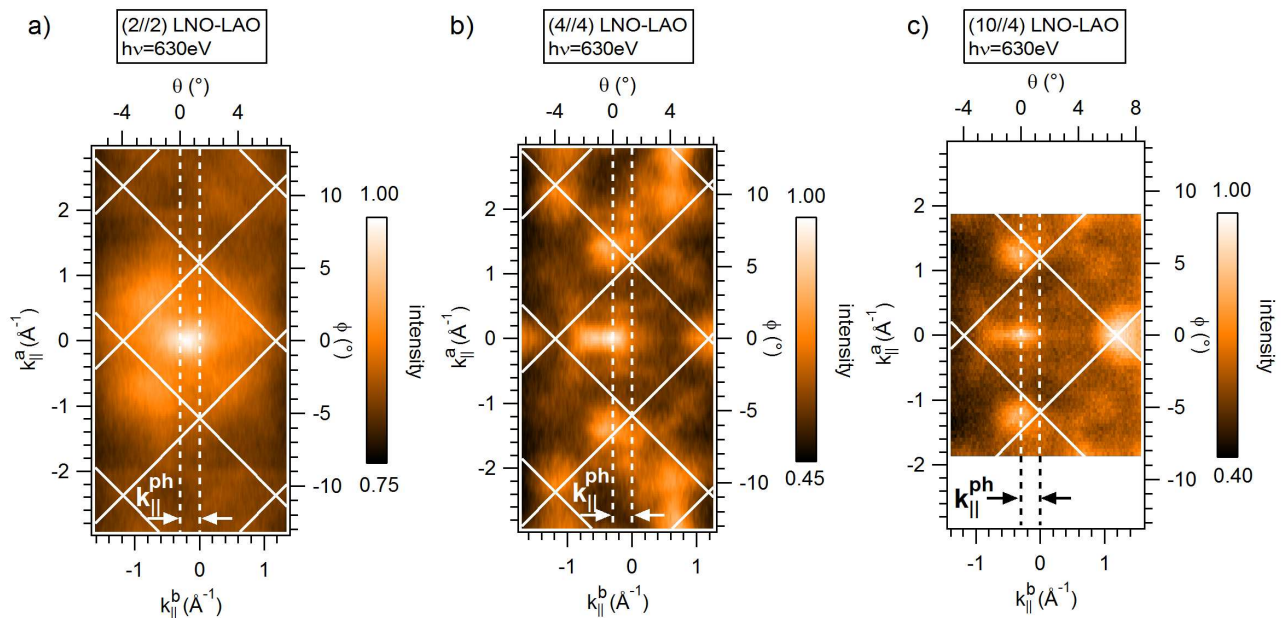


FIG. 7. (Color online) The angle-resolved intensity distribution maps of different LNO/LAO SL at E_F , measured at $h\nu = 630$ eV, which corresponds to $k_z = 0$ \AA^{-1} . The white lines denote the BZ borders. (a) The data taken on the (2//2) SL shows intensity at $k_{\parallel}^{a,b} = 0$ \AA^{-1} , which may be assigned to the electron pocket, slightly interfering with the XPD-induced intensity maximum at $\theta = 0^\circ$. The measured intensity distribution maps of the (b) (4//4) SL and (c) (10//4) SL are dominated by XPD effects. No electron pocket can be identified.

sibly leads to a strongly reduced Ni d_{z^2} occupancy in our samples can most likely be excluded.

Another explanation is a much stronger XPD effect in the SL samples compared to bare LNO films. The data of both the (4//4)-SL and the (10//4) SL in Fig. 7 (b) and (c), respectively, show nearly identical intensity patterns, despite their different LNO layer thickness. They share however the same thickness of the LAO capping layer, and therefore it seems likely that most of the detected intensity modulations are caused by photoelectron diffraction within that layer. In SX-ARPES of bulk LNO films most of the Ni $3d$ signal will originate from the top surface layers, whereas in LAO-capped SLs the photoelectron wave excited from the buried LNO layers will have to pass through the LAO overlayer and thus be subject to *additional* scattering and interference effects. The stronger XPD intensity modulations may then distort or even obscure any underlying k -dependent bandstructure information. A test of this hypothesis would require a more systematic study of SL samples with varying LAO capping layer thickness.

A very clear and unambiguous result of our SX-ARPES study is the change in the microscopic electronic structure from the (4//4) SL to the (2//2) SL, indicating a significant loss of QP coherence concomitant with the dimension-controlled MI-cross-over observed in transport. Different mechanisms have been proposed to explain the latter. For ultra-thin LNO films 2D Anderson localization has been discussed⁸, while other studies performed on ultra-thin films¹³ and SLs²², both under

tensile strain, attribute the insulating phase to charge disproportionation in the two-dimensional ground state. Recent theoretical studies found strong evidence for a magnetic instability, *i.e.* the formation of a spin density wave (SDW), driven by FS nesting, with a wave vector $\mathbf{Q}_{SDW} = 2\pi(\frac{1}{4}, \frac{1}{4}, \frac{1}{4})$ as determined from the theoretical susceptibility.^{20,21} This scenario is supported by spectroscopic data on PrNiO₃-PrAlO₃ superlattices.⁴⁵ Experimentally, muon-spin-rotation¹² and resonant x-ray diffraction experiments¹⁷ indeed observed antiferromagnetic ordering at the predicted wavevector, but only in the (2//2) SL, independent of the used substrate, *i.e.*, the induced strain. SLs with thicker LNO layers exhibit paramagnetic behavior, indicating that the SDW is closely linked to the reduced dimensionality.

Our measured spectroscopic data, especially on the FS topology, provide further support for the SDW scenario. Despite the pronounced loss of coherent quasiparticle weight in the (2//2) SL, the residual intensity modulation in the momentum distribution function $n(\vec{k})$ reproduces a nearly quadratic shape of the FS hole pockets, with flat contours providing a good basis for strong FS nesting. Within experimental resolution the wavevector predicted for the ideal two-dimensional case ($\mathbf{Q}_{SDW} = 2\pi(\frac{1}{4}, \frac{1}{4}, 0)$) is indeed compatible with nesting of the experimental FS [see arrows in Fig. 6 (b)]. On the other hand, it may seem surprising that FS signal can still be observed in our low-temperature data, *i.e.* well within the SDW phase, because a nesting instability would normally open a gap and destroy the FS. However, as already seen in the

EDCs of the (2//2) SL, there is no full gap opening at E_F , at least within our experimental resolution. This behavior could be attributed to an insufficient SDW stabilization due to pronounced order parameter fluctuations, not fully unexpected in the two-dimensional limit. This picture is supported by very recent magneto-resistivity measurements performed on similar LNO/LAO SLs.²⁶ Hepting *et al.*⁴⁵ also find that the SDW state remains metallic, i.e. the gap does not encompass the entire FS. Order parameter fluctuations may also explain the suppression of quasiparticle coherence and the absence of SDW-induced band backfolding, in remarkable contrast to recent ARPES results on ultra-thin films.¹⁰

V. CONCLUSIONS

In summary, we have investigated the electronic structure of compressively strained LNO/LAO SLs grown on LSAO substrates by angle-resolved soft x-ray photoemission. k -integrated valence band spectra show a loss of quasiparticle coherence below 3 uc LNO layer thickness. Corresponding transport measurements exhibit a temperature dependent MI crossover in the (2//2) SL, while the (4//4) and (10//4) SLs stay metallic down to low temperatures.

Although the analysis of the angle-resolved measurements is complicated by strong XPD-induced intensity modulations, the measured angle-resolved maps reveal a dimensional crossover of the FS from three-dimensional in the (4//4) SL to two-dimensional behavior in the (2//2) SL. By comparing the maps with results from DFT calculations, the Ni $d_{x^2-y^2}$ states, which form the hole states around the A points, are clearly identified in the FS of all measured SLs. Evidence for the electron pocket derived from Ni d_{z^2} orbital is found only in the (2//2) SL, but could not be observed for SLs with thicker LNO and LAO layers. We attribute this to pronounced XPD effects in the LAO overlayer, which interfere with or even obscure k -dependent Fermi surface information.

The measured FS topology, in particular the shape of hole pockets in the (2//2) SL, support FS nesting. This is consistent with the scenario of a dimensionality-induced SDW-instability, with the nesting properties of our experimental FS in excellent agreement with the reported SDW wavevector. Thus, our results strongly support magnetic ordering in the two-dimensional ground state of ultra-thin LNO layers embedded in a SL. In line with other experimental as well as theoretical studies, no indication of correlation-induced FS modifications was found for the SLs under compressive strain. Further studies, particularly on LNO/LAO SLs under *tensile* strain, are needed to investigate the tuneability of the electronic structure by strain *and* correlation effects in the two-dimensional limit.

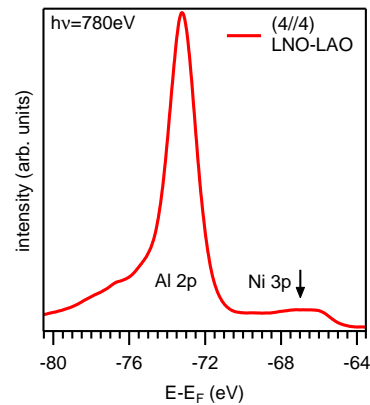


FIG. 8. (Color online) Core-level spectrum including the Al 2*p* and Ni 3*p* line taken at $h\nu = 780$ eV. From the position of the Al 2*p* line the valence band offset of the LAO overlayer is determined. The arrow indicates the binding energy used for the angle-resolved core-level map in Fig. 5 (c).

Appendix A: Valence band offset of the LaAlO₃ overlayer

In the SLs the LNO layer is buried below a LAO capping layer. Thus, the measured valence band is a superposition of the LAO and LNO valence states. Only, if the valence band maximum of the insulating LAO, $E_{\text{VBM}}^{\text{LNO/LAO}}$, is far enough below the Fermi level E_F , the observed spectral weight near E_F can unambiguously be assigned to the Ni 3*d* states in the LNO layers. $E_{\text{VBM}}^{\text{LNO/LAO}}$ is determined by analyzing the position of a suitable core level from LAO, *e.g.* Al 2*p*, and comparing its position with a reference system containing LAO, where core-level position and valence band onset are well known. Here, we use as reference the well-studied LaAlO₃/SrTiO₃ heterostructure with $E_{\text{Al}2p}^{\text{LAO/STO}} \approx -74.35$ eV and $E_{\text{VBM}}^{\text{LAO/STO}} \approx -3.1$ eV (Ref. 46). The energy position of the Al 2*p* core level in the LNO/LAO SLs is found to be $E_{\text{Al}2p} = -73.20$ eV [see Fig. 8], independent of the LAO and LNO layer thickness. From the obvious relationship

$$E_{\text{VBM}}^{\text{LNO/LAO}} = E_{\text{Al}2p}^{\text{LNO/LAO}} - E_{\text{Al}2p}^{\text{LAO/STO}} + E_{\text{VBM}}^{\text{LAO/STO}} \quad (\text{A1})$$

we determine the position of the valence band maximum in the LAO overlayer as $E_{\text{VBM}}^{\text{LNO/LAO}} = -1.95 \pm 0.1$ eV. Consequently, any spectral weight measured between E_F and ≈ -2 eV can only result from the Ni 3*d* states in the LNO layers.

Appendix B: k_z -dependence for bulk LaNiO₃

The relationship between the kinetic energy of the photoelectrons and the momentum perpendicular to the sample surface is described by the following equation includ-

ing the non-negligible photon momentum component k_{\perp}^{ph} [see Fig. 5 (g)]:

$$k_z = \sqrt{2m_e/\hbar^2 (V_0 + E_k \cos^2 \theta)^{1/2} - k_{\perp}^{\text{ph}}, \quad (\text{B1})$$

where m_e is the free electron mass, V_0 the inner potential, E_k the kinetic energy, and θ the emission angle. For thick LNO films a value of $V_0 = 10$ eV has been reported.²⁷ We do not expect a large variation of this phenomenological parameter for our LNO/LAO SLs. Thus, by using the lattice constant perpendicular to the surface $c = 3.840\text{\AA}$ (Ref. 18) and taking the experimental

geometry into account, the photon energies required for probing Fermi level states at the center ($k_z = 0 \text{\AA}^{-1}$) and the edge of the BZ ($k_z = \frac{\pi}{c}$) perpendicular to the surface are $h\nu = 630$ eV and $h\nu = 710$ eV, respectively.

ACKNOWLEDGMENTS

We thank C.S. Fadley and A.X. Gray for fruitful discussions. This work was supported by the Deutsche Forschungsgemeinschaft (FOR 1162) and the German Federal Ministry for Education and Research (05K10WW1).

-
- ¹ H. Y. Hwang, Y. Iwasa, M. Kawasaki, B. Keimer, N. Nagaosa, and Y. Tokura, *Nature Mater.* **11**, 103 (2012).
- ² J. B. Torrance, P. Lacorre, A. I. Nazzari, E. J. Ansaldo, and C. Niedermayer, *Phys. Rev. B* **45**, 8209 (1992).
- ³ M. Imada, A. Fujimori, and Y. Tokura, *Rev. Mod. Phys.* **70**, 1039 (1998).
- ⁴ J. Chaloupka and G. Khaliullin, *Phys. Rev. Lett.* **100**, 016404 (2008).
- ⁵ P. Hansmann, X. Yang, A. Toschi, G. Khaliullin, O. K. Andersen, and K. Held, *Phys. Rev. Lett.* **103**, 016401 (2009).
- ⁶ P. Hansmann, A. Toschi, X. Yang, O. K. Andersen, and K. Held, *Phys. Rev. B* **82**, 235123 (2010).
- ⁷ R. Scherwitzl, P. Zubko, C. Lichtensteiger, and J.-M. Triscone, *Appl. Phys. Lett.* **95**, 222114 (2009).
- ⁸ R. Scherwitzl, S. Gariglio, M. Gabay, P. Zubko, M. Gibert, and J.-M. Triscone, *Phys. Rev. Lett.* **106**, 246403 (2011).
- ⁹ E. Sakai, M. Tamamitsu, K. Yoshimatsu, S. Okamoto, K. Horiba, M. Oshima, and H. Kumigashira, *Phys. Rev. B* **87**, 075132 (2013).
- ¹⁰ H. K. Yoo, S. Ill Hyun, L. Moreschini, Y. J. Chang, D. W. Jeong, C. H. Sohn, Y. S. Kim, H.-D. Kim, A. Bostwick, E. Rotenberg, J. H. Shim, and T. W. Noh, *ArXiv e-prints* (2013), arXiv:1309.0710 [cond-mat.str-el].
- ¹¹ E. Benckiser, M. W. Haverkort, S. Brück, E. Goering, S. Macke, A. Frañó, X. Yang, O. K. Andersen, G. Cristiani, H.-U. Habermeier, A. V. Boris, I. Zegkinoglou, P. Wochner, H.-J. Kim, V. Hinkov, and B. Keimer, *Nature Mater.* **10**, 189 (2011).
- ¹² A. V. Boris, Y. Matiks, E. Benckiser, A. Frano, P. Popovich, V. Hinkov, P. Wochner, M. Castro-Colin, E. Detemple, V. K. Malik, C. Bernhard, T. Prokscha, A. Suter, Z. Salman, E. Morenzoni, G. Cristiani, H.-U. Habermeier, and B. Keimer, *Science* **332**, 937 (2011).
- ¹³ J. Chakhalian, J. M. Rondinelli, J. Liu, B. A. Gray, M. Kareev, E. J. Moon, N. Prasai, J. L. Cohn, M. Varela, I. C. Tung, M. J. Bedzyk, S. G. Altendorf, F. Strigari, B. Dabrowski, L. H. Tjeng, P. J. Ryan, and J. W. Freeland, *Phys. Rev. Lett.* **107**, 116805 (2011).
- ¹⁴ A. M. Kaiser, A. X. Gray, G. Conti, J. Son, A. Greer, A. Perona, A. Rattanachata, A. Y. Saw, A. Bostwick, S. Yang, S.-H. Yang, E. M. Gullikson, J. B. Kortright, S. Stemmer, and C. S. Fadley, *Phys. Rev. Lett.* **107**, 116402 (2011).
- ¹⁵ A. X. Gray, A. Janotti, J. Son, J. M. LeBeau, S. Ueda, Y. Yamashita, K. Kobayashi, A. M. Kaiser, R. Sutarto, H. Wadati, G. A. Sawatzky, C. G. Van de Walle, S. Stemmer, and C. S. Fadley, *Phys. Rev. B* **84**, 075104 (2011).
- ¹⁶ J. W. Freeland, J. Liu, M. Kareev, B. Gray, J. W. Kim, P. Ryan, R. Pentcheva, and J. Chakhalian, *Europhys. Lett.* **96**, 57004 (2011).
- ¹⁷ A. Frano, E. Schierle, M. W. Haverkort, Y. Lu, M. Wu, S. Blanco-Canosa, U. Nwankwo, A. V. Boris, P. Wochner, G. Cristiani, H. U. Habermeier, G. Logvenov, V. Hinkov, E. Benckiser, E. Weschke, and B. Keimer, *Phys. Rev. Lett.* **111**, 106804 (2013).
- ¹⁸ M. Wu, E. Benckiser, M. W. Haverkort, A. Frano, Y. Lu, U. Nwankwo, S. Brück, P. Audehm, E. Goering, S. Macke, V. Hinkov, P. Wochner, G. Cristiani, S. Heinze, G. Logvenov, H.-U. Habermeier, and B. Keimer, *Phys. Rev. B* **88**, 125124 (2013).
- ¹⁹ M. J. Han, X. Wang, C. A. Marianetti, and A. J. Millis, *Phys. Rev. Lett.* **107**, 206804 (2011).
- ²⁰ S. B. Lee, R. Chen, and L. Balents, *Phys. Rev. Lett.* **106**, 016405 (2011).
- ²¹ S. B. Lee, R. Chen, and L. Balents, *Phys. Rev. B* **84**, 165119 (2011).
- ²² J. Liu, S. Okamoto, M. van Veenendaal, M. Kareev, B. Gray, P. Ryan, J. W. Freeland, and J. Chakhalian, *Phys. Rev. B* **83**, 161102 (2011).
- ²³ J. Hwang, J. Son, J. Y. Zhang, A. Janotti, C. G. Van de Walle, and S. Stemmer, *Phys. Rev. B* **87**, 060101 (2013).
- ²⁴ S. J. May, J.-W. Kim, J. M. Rondinelli, E. Karapetrova, N. A. Spaldin, A. Bhattacharya, and P. J. Ryan, *Phys. Rev. B* **82**, 014110 (2010).
- ²⁵ S. J. May, C. R. Smith, J.-W. Kim, E. Karapetrova, A. Bhattacharya, and P. J. Ryan, *Phys. Rev. B* **83**, 153411 (2011).
- ²⁶ D. P. Kumah, A. S. Disa, J. H. Ngai, H. Chen, A. Malashevich, J. W. Reiner, S. Ismail-Beigi, F. J. Walker, and C. H. Ahn, *Adv. Mat.* **26**, 1935 (2014).
- ²⁷ R. Eguchi, A. Chainani, M. Taguchi, M. Matsunami, Y. Ishida, K. Horiba, Y. Senba, H. Ohashi, and S. Shin, *Phys. Rev. B* **79**, 115122 (2009).
- ²⁸ P. D. C. King, I. H. Wei, F. Y. Nie, M. Uchida, C. Adamo, S. Zhu, X. He, I. Bozovic, D. G. Schlom, and M. K. Shen, *Nat. Nanotech.* **9**, 443 (2014).
- ²⁹ G. Berner, M. Sing, H. Fujiwara, A. Yasui, Y. Saitoh, A. Yamasaki, Y. Nishitani, A. Sekiyama, N. Pavlenko,

- T. Kopp, C. Richter, J. Mannhart, S. Suga, and R. Claessen, *Phys. Rev. Lett.* **110**, 247601 (2013).
- ³⁰ V. N. Strocov, X. Wang, M. Shi, M. Kobayashi, J. Krempasky, C. Hess, T. Schmitt, and L. Patthey, *J. Synchrotron Rad.* **21**, 32 (2014).
- ³¹ J. L. García-Muñoz, J. Rodríguez-Carvajal, P. Lacorre, and J. B. Torrance, *Phys. Rev. B* **46**, 4414 (1992).
- ³² A. Frano, E. Benckiser, Y. Lu, M. Wu, M. Castro-Colin, M. Reehuis, A. V. Boris, E. Detemple, W. Sigle, P. van Aken, G. Cristiani, G. Logvenov, H.-U. Habermeier, P. Wochner, B. Keimer, and V. Hinkov, *Adv. Mat.* **26**, 258 (2014).
- ³³ V. N. Strocov, T. Schmitt, U. Flechsig, T. Schmidt, A. Imhof, Q. Chen, J. Raabe, R. Betemps, D. Zimoch, J. Krempasky, X. Wang, M. Grioni, A. Piazzalunga, and L. Patthey, *J. Synchrotron Rad.* **17**, 631 (2010).
- ³⁴ K. Horiba, R. Eguchi, M. Taguchi, A. Chainani, A. Kikkawa, Y. Senba, H. Ohashi, and S. Shin, *Phys. Rev. B* **76**, 155104 (2007).
- ³⁵ N. Hamada, *J. Phys. Chem. Solids* **54**, 1157 (1993).
- ³⁶ D. S. Dessau, T. Saitoh, C.-H. Park, Z.-X. Shen, P. Vilella, N. Hamada, Y. Moritomo, and Y. Tokura, *Phys. Rev. Lett.* **81**, 192 (1998).
- ³⁷ D. Schrupp, M. Sing, M. Tsunekawa, H. Fujiwara, S. Kasai, A. Sekiyama, S. Suga, T. Muro, V. A. M. Brabers, and R. Claessen, *Europhys. Lett.* **70**, 789 (2005).
- ³⁸ C. S. Fadley, *Synchrotron Radiation Research: Advances in Surface Science* (Plenum, New York, 1990).
- ³⁹ C. S. Fadley, *Physica Scripta* **1987**, 39 (1987).
- ⁴⁰ A. X. Gray, J. Minar, L. Plucinski, M. Huijben, A. Bostwick, E. Rotenberg, S.-H. Yang, J. Braun, A. Winkelmann, G. Conti, D. Eiteneer, A. Rattanachata, A. A. Greer, J. Ciston, C. Ophus, G. Rijnders, D. H. A. Blank, D. Doennig, R. Pentcheva, J. B. Kortright, C. M. Schneider, H. Ebert, and C. S. Fadley, *Europhys. Lett.* **104**, 17004 (2013).
- ⁴¹ T. Straub, R. Claessen, P. Steiner, S. Hüfner, V. Eyert, K. Friemelt, and E. Bucher, *Phys. Rev. B* **55**, 13473 (1997).
- ⁴² E. J. Moon, J. M. Rondinelli, N. Prasai, B. A. Gray, M. Kareev, J. Chakhalian, and J. L. Cohn, *Phys. Rev. B* **85**, 121106 (2012).
- ⁴³ M. J. Han, C. A. Marianetti, and A. J. Millis, *Phys. Rev. B* **82**, 134408 (2010).
- ⁴⁴ A. Blanca-Romero and R. Pentcheva, *Phys. Rev. B* **84**, 195450 (2011).
- ⁴⁵ Hepting *et al.*, <http://arxiv.org/abs/1410.8323> (*Phys. Rev. Lett.*, in press).
- ⁴⁶ G. Berner, A. Müller, F. Pfaff, J. Walde, C. Richter, J. Mannhart, S. Thiess, A. Gloskovskii, W. Drube, M. Sing, and R. Claessen, *Phys. Rev. B* **88**, 115111 (2013).